Emergent high-T_c ferroelectric ordering of strongly correlated and frustrated protons in a heteroepitaxial ice film

Toshiki Sugimoto*, Norihiro Aiga, Yuji Otsuki, Kazuya Watanabe and Yoshiyasu Matsumoto*

Materials containing strong correlation and frustration have the potential to respond to external perturbations in an unusual way. In the case of common water ice, protons in the hydrogen-bond network are strongly correlated and highly frustrated under Pauling's ice rules. At low temperature, the strongly correlated protons lose ergodicity, and little is understood about the cooperative thermodynamic and electric response to external stimuli. Here, using a model platinum substrate, we demonstrate emergent high-T_c ferroelectric proton ordering in a heteroepitaxial ice film. Such proton ordering is thermodynamically stable and has an extremely high critical temperature of ∼175 K. We found that anisotropy and protolysis driven by the electrostatistics at the heterointerface are key factors in stimulating this novel exotic ordering in the many-body correlated proton system. The significant increase in T_c due to the heterointerface suggests the ubiquity of ferroelectric ice in nature—specifically, in space and the polar stratosphere.

Water is ubiquitous in nature and its protons in hydrogen-bond (HB) networks play key roles in a variety of disciplines, including physics, chemistry and biology. In common water ice (ice Ih), water molecules constitute a peculiar tetrahedral network with highly asymmetric local structures of protons in hydrogen bonds, where strong correlation and three-dimensional geometrical frustration are intrinsically created under the Bernal–Fowler–Pauling ice rules: each pair of oxygen atoms holds one proton and two protons are closely located at each oxygen[1-4]. Because the strongly correlated protons have an extremely long dielectric relaxation time and lose ergodicity at low temperature, disordered proton structures are inevitably frozen as a protonic glass upon cooling, resulting in a finite macroscopic residual entropy. Unveiling deeply hidden protonic ordered states in crystalline ice (CI) has thus been a longstanding challenge in condensed matter science[1-8]. The traditional way to explore protonic ordering is to chemically dope acidic or basic substances that catalyse proton rearrangement in ice at low temperature. Nowadays, ice XI (ref. 5) is the only phase with ferroelectric ordering among more than fifteen phases of bulk CI (refs 7,8), although the mechanism and energetics in the ferroelectric transition are still under intense debate[4,7-11].

As a straightforward way of fabricating ferroelectric ice, a possibility of interface-induced ferroelectric proton ordering[12] was pointed out in conventional sum-frequency generation (SFG) spectroscopy[6] of CI films grown epitaxially at low coverage on Pt(111). In contrast, surface-voltage measurements with the Kelvin probe technique failed to observe any appreciable surface-voltage build-up during the multilayer growth of epitaxial CI films, including those on Pt(111)[13-16]. Thus, it has been concluded that these CI films are paraelectric and the increase in the SFG signal observed in the previous SFG study on Pt(111)[6] is caused merely by the increase in surface area accompanied by the growth of paraelectric CI clusters on Pt(111)[15]. Consequently, the emergence of interface-induced ferroelectricity in CI films has been considered improbable[15,17,18].

In the case of a strongly correlated electron system, typical proper displacive ferroelectrics are unable to be polarized spontaneously normal to the surface due to the depolarization field; screening of the field is essential to develop stable ferroelectric polarization[19,20]. Because the surface voltages of thin films could be reduced significantly by the screening[19-21], the small surface-voltage build-up reported in the previous Kelvin probe measurements[13-16] may not be direct evidence of the growth of paraelectric CI films, if the field screening also takes place effectively. Thus, whether or not inversion-symmetry breaking at the interface can induce ferroelectric ordering in strongly correlated proton system such as ice is still an open question. To settle this issue, we have investigated epitaxial CI films on a prototype Pt(111) substrate using recently developed phase-sensitive SFG spectroscopy with heterodyne detection[22,23].

SFG is governed by the second-order nonlinear susceptibility $\chi^{(2)}$, which takes nonzero values in media with a net polarization orientation[22,23]. Thus, SFG is a powerful method for studying ferroelectric ordering in bulk materials in addition to surfaces and interfaces. In infrared–visible SFG governed by the vibrationally resonant nonlinear susceptibility $\chi_v^{(2)}$, photons with a sum frequency at $\omega_{IR} + \omega_{VIS}$ are effectively generated when infrared (IR) photons at a frequency of ω_{IR} are near resonant with the transition energy of a vibrational mode in a polarized medium (Fig. 1). In the present system, $\chi_v^{(2)}$ depends on ensemble averages of the polar orientation angle (θ) of the water molecules: $\langle\cos\theta\rangle$ and $\langle\cos^3\theta\rangle$. Although $|\chi_v^{(2)}|^2$ spectra obtained with the conventional homodyne-detected SFG[6,17,24] show a positive sign regardless of the orientation of the water molecules, $\text{Im}\chi_v^{(2)}$ spectra obtained by the heterodyne-detected SFG exhibit a positive or negative sign for a net orientation of OH, with hydrogen pointing away from or towards Pt(111), respectively (Supplementary Sections 1 and 2). Thus, heterodyne-detected SFG has a great advantage in directly observing the local configuration of protons that cannot be investigated through other traditional experimental methods.

Department of Chemistry, Graduate School of Science, Kyoto University, Kyoto 606-8502, Japan. *e-mail: toshiki@kuchem.kyoto-u.ac.jp; matsumoto@kuchem.kyoto-u.ac.jp
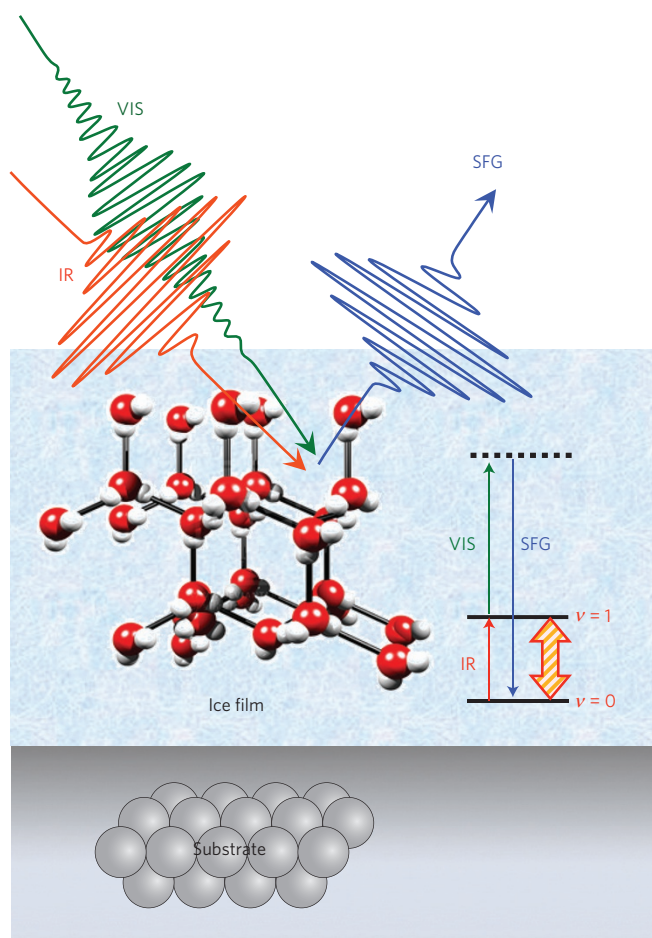
Figure 1 | Schematic illustration of *in situ* infrared–visible sum-frequency generation (SFG) spectroscopy of a heteroepitaxial ice film. Due to the second-order nonlinear optical effects, incident visible (VIS) and infrared (IR) light generate sum-frequency light in the ferroelectric domain with a net orientational preference. SFG is significantly enhanced when the incident IR light resonantly excites a subset of water molecules from the ground vibrational state ($v = 0$) to the first excited vibrational state ($v = 1$).

Figure 2a shows $|\chi_v^{(2)}|^2$ spectra of HDO crystalline-ice films deposited on Pt(111) at 140 K as a function of the adsorbed amount Φ (Methods). The intensities of $|\chi_v^{(2)}|^2$ for the hydrogen-bonded OH- and OD-stretch bands increase monotonically with Φ, without saturation: $|\chi_v^{(2)}|^2 \propto \Phi^m$: $m \sim 2$ for $\Phi < {\sim}30$ ML and $m = 1$ for $\Phi > {\sim}30$ ML (Fig. 2b). The same Φ dependence of $|\chi_v^{(2)}|^2$ was observed during the growth of H_2O and D_2O crystalline-ice films. Although a previous SFG study has claimed that the amplitude of $|\chi_v^{(2)}|$ is saturated at a characteristic decay thickness of 30 ML, based on the results in a limited low-coverage range[6], our results over a much wider coverage range clearly show that $|\chi_v^{(2)}|$ continues to increase on Pt(111) as $|\chi_v^{(2)}| \propto \Phi^{1/2}$ for thick CI films (Fig. 2b). If ferroelectric proton ordering were perfectly propagated without decay during the film growth, $|\chi_v^{(2)}|$ itself would continue to linearly increase as $|\chi_v^{(2)}| \propto \Phi$. Thus, the observed coverage dependence $|\chi_v^{(2)}| \propto \Phi^m$ with $m = 1/2 < 1$ for a thick coverage region suggests that the ferroelectric ordering decays gradually in the upper ice layer.

To verify in which direction protons preferentially orient in the film, we measured $\mathrm{Im}\chi_v^{(2)}$ spectra (Fig. 2c). A single negative peak was observed at around 3,370 cm^{-1} at $\Phi < 1$ ML, followed by a new negative peak at around 3,275 cm^{-1} that continued to grow with further multilayer adsorption (Fig. 2c,d). The negative sign of $\mathrm{Im}\chi_v^{(2)}$ for the first layer clearly indicates that water molecules just above

Pt(111) have a net orientational preference of one of their hydrogen pointing toward the substrate, in good agreement with the structure predicted by density functional theory (DFT) calculations[25,26]— that is, the $(\sqrt{39} \times \sqrt{39})R16.1°$ first-layer superstructure with H-down orientation. In contrast to the theoretical predictions[18,26], however, there is no appreciable adsorption-induced conversion in orientation for the first-layer water molecules—that is, flipping from H-down to H-up orientation—because the negative intensity of the OH-stretch band for the first-layer molecules is unchanged during the multilayer film growth (Fig. 2c,d). Our results thus demonstrate that the H-down proton ordering in the first layer is significantly pinned by the Pt(111) substrate, and is subsequently propagated to the overlayer during the CI film growth.

Previous studies have shown that the growth behaviour of multilayer CI films changes from the Stranski–Krastanov (SK) to the quasi-continuous layer-by-layer (QCLL) mode on Pt(111)[27,28]. Because the increase in surface area accompanied by the growth of paraelectric CI clusters would also contribute to the increase in the SFG signal, the growth behaviour of CI films should be taken into account for a solid verification of the growth of ferroelectric CI. The transition from SK to QCLL growth on Pt(111)[27,28] is reasonably modelled as a function of Φ (Fig. 3a) with the following relation: $\Phi = a + h(1 - a)$, where h and a denote the average height of crystallites and the fraction of molecules in the first layer exposed to vacuum, respectively, both in units of ML. Figure 2b shows that $|\chi_v^{(2)}|$ continues to increase with $\sqrt{\Phi}$ for the growth of QCLL CI films, with $a = 0$ at larger $\Phi (=h)$. Because the surface area of the QCLL CI films is constant, and thus surface-derived SFG should be constant for QCLL CI films, this result clearly indicates that the observed increase in the SFG signals originates not from the increase in surface area of paraelectric CI clusters but from the growth of ferroelectric CI with net-H-down proton ordering.

As clearly described in Supplementary Section 1, $\chi_v^{(2)}$ is proportional to the sum of the degree of net orientational ordering p_n in the nth layer: $\chi_v^{(2)}(\Phi) \propto \sum_{n=1}^{\Phi} p_n$. Therefore, taking the derivative of the following simple relation with respect to Φ, $-\Phi^{1/2} \propto \sum_{n=1}^{\Phi} p_n \sim \int_1^{\Phi} p_n \, dn$, and replacing Φ with n result in $p_n \propto -n^{-1/2}$—that is, $p_n = p_1/\sqrt{n}$ with $p_1 < 0$ (Fig. 3b). In this case, p_n satisfies the following recurrence equation for the layer-by-layer propagation of the proton ordering: $p_{n+1} = \alpha_n p_n$ ($n \geq 1$), where $\alpha_n = \sqrt{n/(n+1)}$. Note that the dependence of the SFG intensity on the adsorbed amount for $\Phi < {\sim}30$ ML had a convex down curvature as $|\chi_v^{(2)}|^2 \propto \Phi^2$ (Fig. 2b), which apparently contradicts the result that $|\chi_v^{(2)}|^2 \propto \Phi$ for $\Phi > {\sim}30$ ML. As discussed below, the apparently distinct dependence of the SFG intensity on the adsorbed amount would be a manifestation of the difference in the growth mode of CI. If the same polarization propagation behaviour ($p_n = p_1/\sqrt{n}$) is assumed to take place in each crystallite in the SK growth mode at small Φ with $a \neq 0$, the Φ dependence of $\chi_v^{(2)}$ is described as follows.

$$\chi_v^{(2)}(\Phi) \propto p_1 + (1 - a(\Phi)) \sum_{n=2}^{h(\Phi)} p_n$$

$$\propto p_1 \left[1 + (1 - a(\Phi)) \sum_{n=2}^{h(\Phi)} \frac{1}{\sqrt{n}} \right] \quad (1)$$

Red solid lines shown in Fig. 2b,d show the simulated Φ dependence of $|\chi_v^{(2)}|^2$ and $\mathrm{Im}\chi_v^{(2)}$ based on equation (1) and the Φ-dependent h and a given in Fig. 3a. These curves closely reproduce the observed Φ dependence of both $|\chi_v^{(2)}|^2$ and $\mathrm{Im}\chi_v^{(2)}$, which suggests that even for the 'crystallite growth' regime at small Φ the net-H-down ordering of the nth layer propagates as $p_n = p_1/\sqrt{n}$ ($p_1 < 0$): $p_{n+1} = \alpha_n p_n$, with $\alpha_n = \sqrt{n/(n+1)}$. As shown above, the entire Φ dependence observed in our SFG measurement can be described by a propagation behaviour of ferroelectric
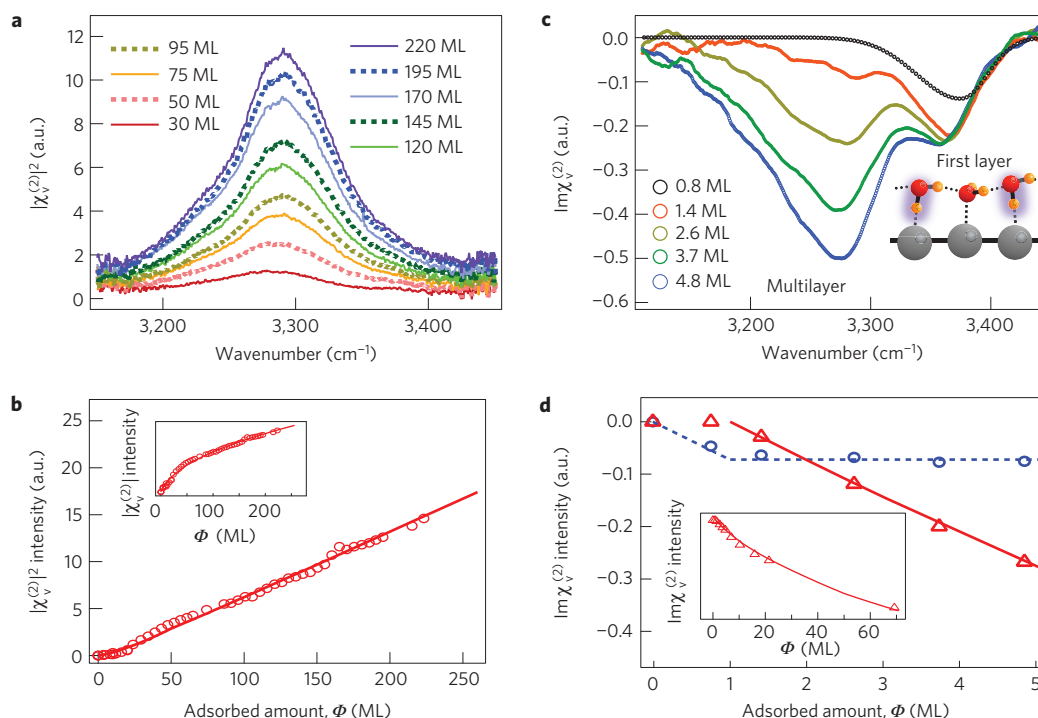
Figure 2 | Infrared–visible sum-frequency generation spectroscopy of crystalline-ice films on Pt(111). a, The $|\chi_v^{(2)}|^2$ spectra of the hydrogen-bonded local OH-stretch band of HDO crystalline-ice films deposited on Pt(111) at 135 K. Horizontal axis is the wavenumber of the incident broadband IR laser pulses. **b**, Dependence on the adsorbed amount Φ of the $|\chi_v^{(2)}|^2$ intensity (circle) and the result of curve fitting by equation (1) (solid line) with parameters a and h given in Fig. 3a. Inset: Φ dependence of the $|\chi_v^{(2)}|$ intensity and the result of curve fitting by $\sqrt{\Phi}$. **c**, The $\mathrm{Im}\chi_v^{(2)}$ spectra obtained from heterodyne-detected SFG for HDO crystalline-ice films with low Φ. A slight non-resonant background[23,24] was subtracted from these spectra. **d**, Φ dependence of the negative $\mathrm{Im}\chi_v^{(2)}$ intensity for the first-layer peak (blue circles) and multilayer peak (red triangles). Blue dashed and red solid lines are guides for the eye and the result of curve fitting based on equation (1) and Fig. 3a, respectively.

ordering given as $p_n = p_1/\sqrt{n}$ and the transition of the growth mode of CI from the SK to QCLL mode (Fig. 3a).

The inset of Fig. 3c shows the n dependence of the coefficient α_n, which increases drastically with n at <10 ML, before gradually converging to 1 at large n. If the short-range constraint of the ice rules were strictly hold, the protonic ordering would be perfectly propagated from a layer to overlayers as $p_{n+1} = p_n$ with $\alpha_n = 1$. Thus, the deviation of α_n from 1 indicates that the ice rules are violated, in particular, in the film near the Pt(111) substrate (Fig. 3c).

Regardless of the substantial net ferroelectric proton ordering in the CI film, we could not observe any appreciable peak shift due to static-voltage build-up[29] in the O 1s X-ray photoelectron spectrum at ~533.5 eV (ref. 15) during multilayer growth of the film, which is in good agreement with previous Kelvin probe measurements[13–15]. Such an apparent contradiction can be reasonably reconciled by screening of a depolarization field[19–21] that eliminates ferroelectric instability through a redistribution of the electron density at the ice/Pt(111) heterointerface, as discussed in Supplementary Section 5. The depolarization field would be almost perfectly screened in this case due to the protolysis at the interface and in the film. Based on the results observed, we estimate the possible net-H-down orientational polarization for the nth layer in the unscreened ferroelectric CI film as $P_n = -8.7 \times 10^{-2}/\sqrt{n}$ [C m^{-2}] (Supplementary Section 5). The net-H-down polarization would result in a net negative polarization-charge density $\sigma_n^{\mathrm{pol}} = -4.4 \times 10^{-2}/\sqrt{n^3}$ [C m^{-2}] in the film and induce significant upward band bending of $+7.2\sqrt{n}$ [eV] (Supplementary Fig. 6). Due to the band bending, electrons in the valence band above the Fermi level of Pt(111) spontaneously transfer from the CI film to the substrate, thus eliminating the instability and equilibrating the chemical potential. As a result, holes are injected in the

film near the interface. Because holes would be stabilized as hydronium cations through subtraction of H atoms from the neighbouring water molecules as $H_2O^+ + H_2O \rightarrow H_3O^+ + OH$ (refs 30,31) and the hydronium cations (protons) are mobile in HB networks[1,30], they would be redistributed in the film to screen the negative polarization charge and remove ferroelectric instability. Thus, the small work-function change reported in the Kelvin probe measurements[13,14], indicating almost perfect screening of the negative polarization charges, provides the distribution of hydronium cations as $\sigma_n^{H_3O^+} = -\sigma_n^{\mathrm{pol}} = 4.4 \times 10^{-2}/\sqrt{n^3}$ [C m^{-2}] for the nth layer. The relative concentration of hydronium cations to neutral water molecules in the nth layer is $[H_3O^+]_n^{\mathrm{rel}} = (\sigma_n^{H_3O^+}/e\bar{N}_{\mathrm{ice}}) \times 100 = 2.8/\sqrt{n^3}$ [%], where $\bar{N}_{\mathrm{ice}} \sim 1.1 \times 10^{19}$ [m^{-2}] (ref. 2). The spontaneously introduced hydronium cations partially violate the ice rules in the film and would induce the randomization of ferroelectric proton ordering during the growth of the ferroelectric CI film. The correspondence between the value of $[H_3O^+]_n^{\mathrm{rel}}$ and $1 - \alpha_n$ is shown in Fig. 3c.

To explore the thermodynamic stability and unique features of the ferroelectric CI films, we conducted simultaneous measurements of homodyne-detected SFG and temperature programmed desorption (TPD)[32] for an epitaxial HDO CI film with a thickness of 330 ML. Although the spectral profile of the OH-stretching band hardly changed (Supplementary Section 6), the intensity decreased with increasing temperature even in the temperature range where sublimation of ice is negligible (Fig. 4a): the SFG intensity is reversibly recovered and decreases again during a sequence of cooling and reheating processes. We note that the intensity of $|\chi_v^{(2)}|$ depends not only on the ferroelectricity derived from the net orientation of water molecules, but also on the hyperpolarizability β, which is proportional to the infrared transition dipole and Raman polarizability[33] (Supplementary Sections 1 and 6). The thin red solid
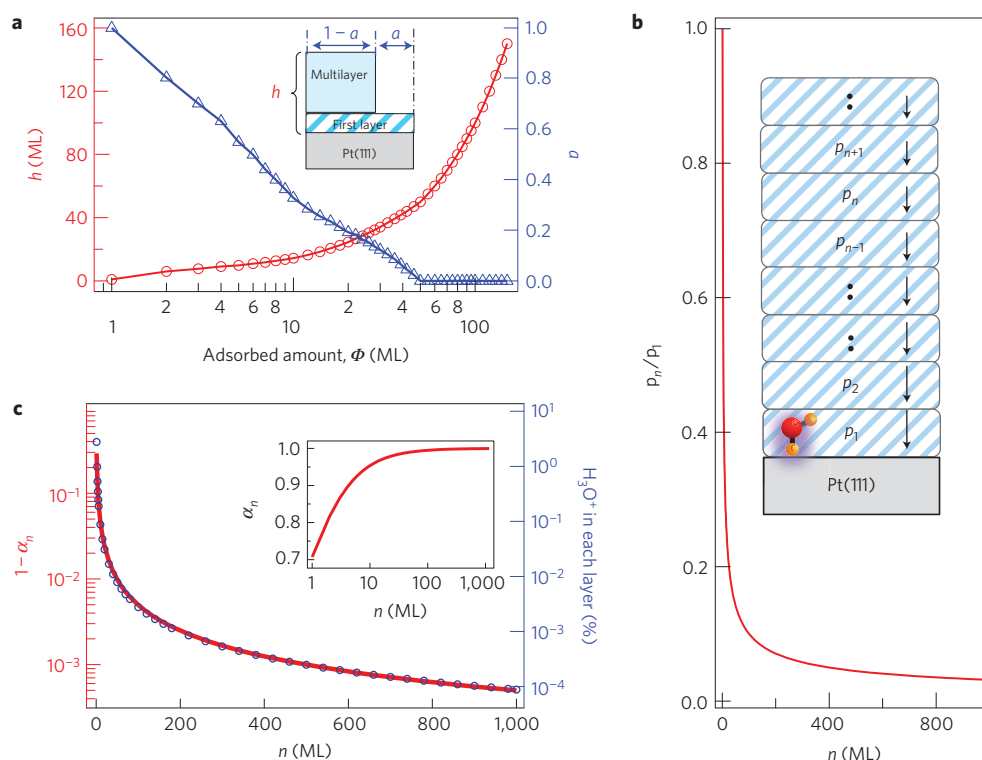
Figure 3 | Growth model of crystalline-ice films, the propagation of net-H-down proton ordering, and partial violation of the ice rules on Pt(111).
a, Dependence on the adsorbed amount Φ of the fraction of the first layer exposed to vacuum a (ref. 27), and the average crystallite height h derived from the relation $\Phi = a + h(1 - a)$. These parameters closely reproduce the average features of the transition from the Stranski–Krastanov to the quasi-continuous layer-by-layer growth mode of crystalline-ice films on Pt(111)[28]. **b**, Net-H-down orientational ordering for each nth layer $p_n = p_1/\sqrt{n}$ normalized by p_1 (<0) as a function of n. **c**, The n dependence of α_n (inset) and the correlation between $1 - \alpha_n$ and the relative concentration of hydronium cations to neutral water molecules in the nth layer.

line shown in Fig. 4a is a simulated temperature dependence of $|\chi_v^{(2)}|$ estimated only from the possible temperature dependence of β (Supplementary Section 6). Good agreement with experimental results below 150 K indicates that the observed change in $|\chi_v^{(2)}|$ below 150 K is mainly derived from the temperature dependence of β.

In contrast, $|\chi_v^{(2)}|$ decreases much more steeply than β above 150 K (Fig. 4a), indicating a substantial ferroelectric–paraelectric transition in the ice film. Above 160 K, sublimation significantly decreases the adsorbed amount of water molecules, which also contributes to the apparent decay in the SFG intensity. To deal with the dependence of $|\chi_v^{(2)}|$ on the adsorbed amount, we introduce a coverage-normalized order parameter $\eta(T) \propto |\chi_v^{(2)}|/\beta\sqrt{\Phi}$, assuming that $|\chi_v^{(2)}|$ can be written in the form of a product of the coverage-dependent term proportional to $\sqrt{\Phi}$ and the temperature-dependent term η (Fig. 4b). Here, the contribution of the temperature dependence of β to $|\chi_v^{(2)}|$ was also corrected. $\eta(T)$ reversibly increased and decreased with temperature in the higher temperature range (Supplementary Fig. 9c): the second-order-like macroscopic ferroelectric–paraelectric transition takes place in thermodynamically equilibrium conditions, in contrast to that of bulk ice XI[1,5,8,9,11] and metastably quenched weakly ferroelectric amorphous ice films[13,34].

In addition, almost the same decay curve of $\eta(T)$ was observed for the CI films with different initial thickness. The size effect is thus negligible for the transition. Curve fitting of $\eta(T)$ to the well-known empirical function $(T_c - T)^\gamma$ for a second-order transition gives a critical temperature $T_c = 173 \pm 1$ K (Fig. 4b), but the quality of the curve fitting is poor. Figure 4b also shows a result of curve fitting with a statistical model[35] of a ferroelectric–paraelectric transition under the short-range

constraint of the ice rules and their partial violation due to the formation of orientational Bjerrum L and D defects[1]; the model closely reproduces the observed transition. The formation energy of an L- and D-defect pair obtained from the curve fitting is 92 ± 5 meV, which is much smaller than that of bulk ice[1]. Because the L and D defects are negatively and positively electrified[1], respectively, hydronium cations spontaneously introduced in the film during the deposition process would efficiently split these defect pairs by trapping L defects preferentially[30,36]. The stabilization of L defects and the resultant local structure distortion would cause effective lowering of the apparent defect-formation energy[30,36]. Weakening of the proton correlation in ice through partial violation of the ice rules promotes unimolecular reorientation of water molecules (Fig. 4c,d), inducing a second-order-like ferroelectric–paraelectric transition below the critical temperature (Fig. 4b).

In summary, we have unambiguously demonstrated that strongly correlated and highly frustrated many-body protons in crystalline-ice film show an emergent thermodynamic and electric response to symmetry breaking at a heterointerface. The first-layer water molecules strongly pinned in the H-down configuration on Pt(111) lift the degeneracy in the frustrated proton configurations and develop an extremely high-T_c net-H-down ferroelectric ordering in the HB network of overlayers. Our results using a heterogeneous catalyst such as Pt(111) thus open up a new route to unveil the hidden exotic ferroelectric properties of strongly correlated and highly frustrated many-body protons beyond the current phase diagram of crystalline bulk ice[1,7,8]. During the growth of crystalline-ice films, hole injection at the interface producing hydronium cations in ice would be essential to stabilize the strong H-down ferroelectric ordering. The concept
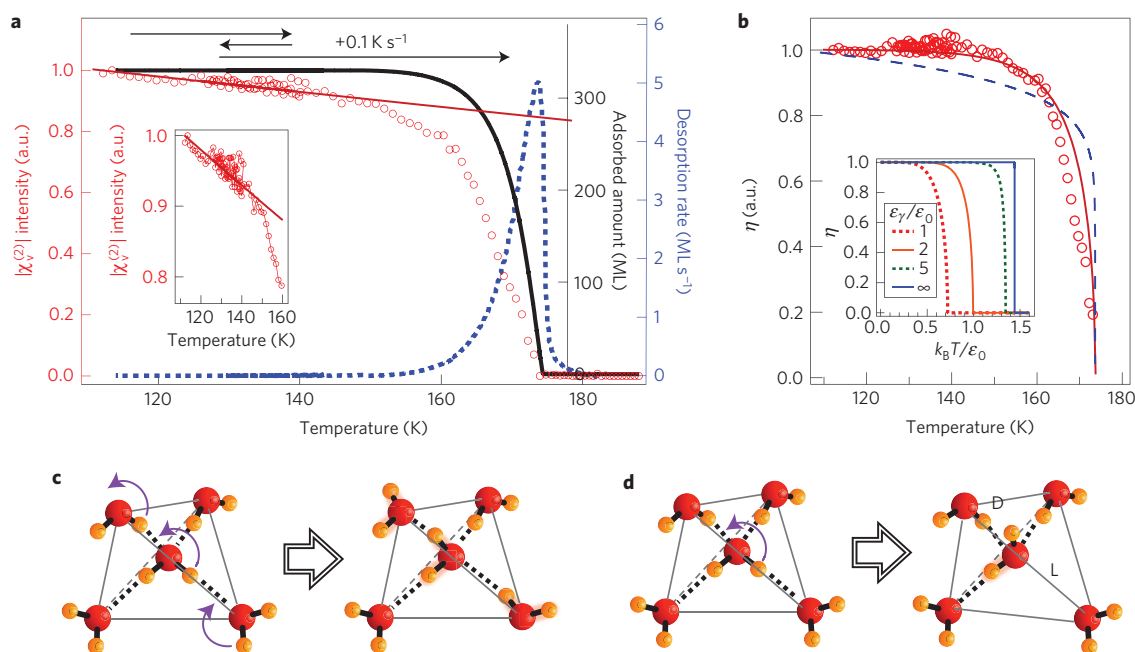
Figure 4 | Effect of ice-rules violation on high-T_c proton ordering. a, Simultaneous measurements of the temperature dependence of $|\chi_v^{(2)}|$ intensity (red open circles) and the desorption rate of HDO molecules (blue dots) for a 330-ML-thick crystalline-ice film on Pt(111) prepared at 135 K. The film was precooled to 110 K. Three horizontal black arrows indicate the temperature ranges of the heating ($+0.10$ K s^{-1}), cooling (-0.05 K s^{-1}) and reheating ($+0.10$ K s^{-1}) processes. Thick black and thin red lines are the adsorbed amount of the film and an estimated decay of $|\chi_v^{(2)}|$ due to the possible temperature dependence of molecular hyperpolarizability (Supplementary Section 6), respectively. Inset: enlarged view of the temperature dependence of $|\chi_v^{(2)}|$ below 160 K. **b,** Order parameter η normalized at ~110 K (red circles). The red solid line is the thermal randomization curve calculated by a statistical theory, taking account of the ice rules and their partial violation[35], with a defect-formation energy of $2\varepsilon_\gamma = 92 \pm 5$ meV and an orientational anisotropic energy of $\varepsilon_0 = 11 \pm 1$ meV. The blue dashed line is a result of curve fitting with an empirical function of $(T_c - T)^\gamma$ with $T_c = 174$ K and $\gamma = 0.10$ shown for comparison. k_B is the Boltzmann constant. Inset: the effect of the defect-formation energy on the thermal randomization of ferroelectric proton ordering. If the cost of defect formation becomes lower, the ferroelectric–paraelectric transition takes place gradually below the critical temperature as a second-order transition due to the weakening of the strongly cooperative rearrangement of the proton configuration. **c,d,** Schematic illustration of water reorientation in the HB network under the strict ice-rules restrictions (**c**) and their partial violation due to an orientational L- and D-defect pair formation (**d**)[1].

of depolarization field screening also has profound implications for the controversy about the role of homogeneous basic catalysts in the ferroelectric transition of bulk ice[1,4,7–11]: the homogeneously distributed dopants would act not only as an accelerator of proton motion but also as a stabilizer eliminating ferroelectric instability in bulk ice XI. Furthermore, our results have crucial consequences for the ubiquity of ferroelectric ice in nature. In space and the polar stratosphere, ice is the most abundant solid substance condensed on dust particles[9,37], where molecular evolution and interconversion between nuclear-spin modifications of particular astro- and atmospheric-physicochemical importance are accelerated on ice[37,38]. The heterointerface-induced increase in T_c for the thermodynamically stable protonic ordering suggests the existence of ferroelectric ice over a much vaster region in space and the polar stratosphere than ever expected from the transition temperature of $T_c \sim 72$ K for ferroelectric bulk ice XI (ref. 9).

Finally, we remark on the following point. We have phenomenologically demonstrated the propagation behaviour of the ferroelectric proton ordering and discussed possible factors that dominate energetics at the interface and in the film, on the basis of our experimental results. However, we have still not reached a quantitative understanding on the microscopic origin of the functional form of $|\chi_v^{(2)}|$, that is, $|\chi_v^{(2)}| \propto \Phi^{1/2}$, and the resultant power-low behaviour of $p_n \propto n^{-1/2}$ for the propagation of ferroelectric ordering. Forthcoming systematic research into CI films on other metal and non-metal surfaces using SFG would provide further insights into the growth mechanism of ferroelectric CI films and the underlying microscopic energetic balance.

Methods

Methods, including statements of data availability and any associated accession codes and references, are available in the online version of this paper.

References

1. Petrenko, V. F. & Whitworth, R. W. *Physics of Ice* (Oxford Univ. Press, 1999).
2. Bramwell, S. T. Ferroelectric ice. *Nature* **397,** 212–213 (1999).
3. Bramwell, S. T. & Gingras, M. J. P. Spin ice state in frustrated magnetic pyrochlore materials. *Science* **294,** 1495–1501 (2001).
4. Neto, A. H. C., Pujol, P. & Fradkin, E. Ice: a strongly correlated proton system. *Phys. Rev. B* **74,** 024302 (2006).
5. Tajima, Y., Matsuo, T. & Suga, H. Phase transition in KOH-doped hexagonal ice. *Nature* **299,** 810–812 (1982).
6. Su, X., Lianos, L., Shen, Y. R. & Somorjai, G. A. Surface-induced ferroelectric ice on Pt(111). *Phys. Rev. Lett.* **80,** 1533–1536 (1998).
7. Salzmann, C. G., Radaelli, P. G., Hallbrucker, A., Mayer, E. & Finney, J. L. The preparation and structures of hydrogen ordered phases of ice. *Science* **311,** 1758–1761 (2006).
8. Salzmann, C. G., Radaelli, P. G., Slater, B. & Finney, J. L. The polymorphism of ice: five unresolved questions. *Phys. Chem. Chem. Phys.* **13,** 18468–18480 (2011).
9. Arakawa, M. *et al.* The existence of memory effect on hydrogen ordering in ice: the effect makes ice attractive. *Geophys. Res. Lett.* **38,** L16101 (2011).
10. Parkkinen, P., Riikonen, S. & Halonen, L. Ice XI: not that ferroelectric. *J. Phys. Chem. C* **118,** 26264–26275 (2014).
11. Yen, F. & Chi, Z. Proton ordering dynamics of H₂O ice. *Phys. Chem. Chem. Phys.* **17,** 12458–12461 (2015).

12. Ryzhkin, I. A. & Petrenko, V. F. Proton ordering in ice at an ice–metal interface. *J. Exp. Theor. Phys.* **101,** 317–321 (2005).

13. Iedema, M. J. *et al*. Ferroelectricity in water ice. *J. Phys. Chem. B* **102,** 9203–9214 (1998).

14. Harnett, J., Haq, S. & Hodgson, A. Electron induced restructuring of crystalline ice adsorbed on Pt(111). *Surf. Sci.* **528,** 15–19 (2003).

15. Hodgson, A. & Haq, S. Water adsorption and the wetting of metal surfaces. *Surf. Sci. Rep.* **64,** 381–451 (2009).

16. McBride, F. *et al*. Strain relief and disorder in commensurate water layers formed on Pd(111). *J. Phys. Condens. Matter* **24,** 124102 (2012).

17. Denzler, D. N. *et al*. Interfacial structure of water on Ru(001) investigated by vibrational spectroscopy. *Chem. Phys. Lett.* **376,** 618–624 (2003).

18. Witek, H. & Buch, V. Structure of ice multilayers on metals. *J. Chem. Phys.* **110,** 3168–3175 (1999).

19. Junquera, J. & Ghosez, P. Critical thickness for ferroelectricity in perovskite ultrathin films. *Nature* **422,** 506–509 (2003).

20. Sai, N., Kolpak, A. M. & Rappe, A. M. Ferroelectricity in ultrathin perovskite films. *Phys. Rev. B* **72,** 020101 (2005).

21. Nie, S., Bartelt, N. C. & Thürmer, K. Evolution of proton order during ice-film growth: an analysis of island shapes. *Phys. Rev. B* **84,** 035420 (2011).

22. Shen, Y. R. Phase-sensitive sum-frequency spectroscopy. *Annu. Rev. Phys. Chem.* **64,** 129–150 (2013).

23. Nihonyanagi, S., Mondal, J. A., Yamaguchi, S. & Tahara, T. Structure and dynamics of interfacial water studied by heterodyne-detected VSFG. *Annu. Rev. Phys. Chem.* **64,** 579–603 (2013).

24. Nagao, M., Watanabe, K. & Matsumoto, Y. Ultrafast vibrational energy transfer in the layers of D_2O and CO on Pt(111) studied with time-resolved sum-frequency-generation spectroscopy. *J. Phys. Chem. C* **113,** 11712–11719 (2009).

25. Meng, S., Wang, E. G. & Gao, S. Water adsorption on metal surfaces: a general picture from density functional theory studies. *Phys. Rev. B* **69,** 195404 (2004).

26. Nie, S., Feibelman, P. J., Bartelt, N. C. & Thürmer, K. Pentagons and heptagons in the first water layer on Pt(111). *Phys. Rev. Lett.* **105,** 026102 (2010).

27. Kimmel, G. A., Petrik, N. G., Dohnálek, Z. & Kay, B. D. Crystalline ice growth on Pt(111): observation of a hydrophobic water monolayer. *Phys. Rev. Lett.* **95,** 166102 (2005).

28. Thürmer, K. & Bartelt, N. C. Nucleation-limited dewetting of ice films on Pt(111). *Phys. Rev. Lett.* **100,** 186101 (2008).

29. Ehre, D. & Cohen, H. Contact-free pyroelectric measurements using X-ray photoelectron spectroscopy. *Appl. Phys. Lett.* **103,** 052901 (2013).

30. Kunst, M. & Warman, J. M. Nanosecond time-resolved conductivity studies of pulse-ionized ice. 2. The mobility and trapping of protons. *J. Phys. Chem.* **87,** 4093–4095 (1983).

31. Mizuse, K., Kuo, J. L. & Fujii, A. Structural trends of ionized water networks: infrared spectroscopy of water cluster radical cations $(H_2O)_n^+$ ($n=3-11$). *Chem. Sci.* **2,** 868–876 (2011).

32. Sugimoto, T. & Fukutani, K. Effects of rotational-symmetry breaking on physisorption of ortho- and para-H_2 on Ag(111). *Phys. Rev. Lett.* **112,** 146101 (2014).

33. Scherer, J. R. & Snyder, R. G. Raman intensities of single crystal ice Ih. *J. Chem. Phys.* **67,** 4794–4811 (1977).

34. Bu, C., Shi, J., Raut, U., Mitchell, E. H. & Baragiola, R. A. Effect of microstructure on spontaneous polarization in amorphous solid water films. *J. Chem. Phys.* **142,** 134702 (2015).

35. Shirane, G. & Oguchi, T. On the transition in KH_2PO_4. *J. Phys. Soc. Jpn* **4,** 172–176 (1949).

36. Watkins, M., VandeVondele, J. & Slater, B. Point defects at the ice (0001) surface. *Proc. Natl Acad. Sci. USA* **107,** 12429–12434 (2010).

37. Hama, T. & Watanabe, N. Surface processes on interstellar amorphous solid water, adsorption, diffusion, tunneling reactions, and nuclear-spin conversion. *Chem. Rev.* **113,** 8783–8839 (2013).

38. Sugimoto, T. & Fukutani, K. Electric-field-induced nuclear-spin flips mediated by enhanced spin–orbit coupling. *Nature Phys.* **7,** 307–311 (2011).

Author contributions

T.S. planned and Y.M. organized the project; K.W. developed the experimental system; T.S., N.A. and Y.O. improved the experimental system and conducted measurements, T.S. analysed the data and wrote the manuscript; all authors discussed the results and commented on the manuscript.

Additional information

Supplementary information is available in the online version of the paper. Reprints and permissions information is available online at www.nature.com/reprints. Correspondence and requests for materials should be addressed to T.S. or Y.M.

Competing financial interests

The authors declare no competing financial interests.

Methods

Preparation of clean Pt(111) substrates. We have used three single-crystal Pt(111) substrates purchased from MaTeck GmbH to confirm reproducibility of the growth of proton-ordered crystalline-ice films on Pt(111). The Pt(111) single-crystal substrates were cleaned by cycles of Ar$^+$ bombardment at 500 eV, annealing at 800 K under an oxygen pressure of 1×10^{-5} Pa, and flushing at 1,050 K in an ultrahigh-vacuum (UHV) environment with a base operating pressure below 5×10^{-8} Pa. The surface cleanliness and structure of the substrates were checked by means of Auger electron spectroscopy (AES), low-energy electron diffraction (LEED), and temperature programmed desorption (TPD) of water, respectively. AES spectra revealed that the substrates were chemically clean, without any trace of oxygen and carbon contaminants; LEED revealed a clear 1×1 pattern with the three-fold symmetry characteristic of a (111) surface of a face-centred cubic structure; TPD measurement of sub-monolayer H_2O molecules deposited through backfill water-vapour deposition on Pt(111) at 135 K showed a quasi-zero-order single desorption peak whose peak top appeared at around 170 K for saturated first-layer H_2O molecules under a heating rate of 1 K s^{-1}; this is in good agreement with previous studies[6,27,39,40]. Note that we have never observed desorption of water at around 200 K, which is originated from the dissociated water molecules on Pt(111)[41–44].

Calibration of adsorbed amount of water molecules by TPD spectra. The amount of water molecules adsorbed on Pt(111) was routinely calibrated with the conventional TPD technique, where the area of each desorption signal was proportional to the amount of adsorbed water molecules. In this paper, the adsorbed amount of water molecules is expressed in the monolayer (ML) unit following the previous studies of water adsorption on Pt(111) surfaces[6,27,39–45]. Here, 1 ML corresponds to the amount of water adsorbed in the saturated first layer with a $(\sqrt{39} \times \sqrt{39})R16.1°$ superstructure[14,25,26,46] on Pt(111) showing the single quasi-zero-order desorption peak at around 170 K (refs 6,27,39,40); this is nearly equivalent to the amount of water molecules in a bilayer (BL) of bulk ice Ih ($\sim 1.1 \times 10^{19}$ m^{-2}) (ref. 1). After further deposition of water molecules, we observed zero-order desorption from a multilayer crystalline-ice film starting above around 137 K, in good agreement with previous studies[6,27,39–45]. The intensity of multilayer desorption peaks was proportional to the dosage amount through backfill water-vapour deposition as well as the intensity of a hydrogen-bonded OH-stretch (OD-stretch) band of water molecules in the crystalline-ice films measured with infrared reflection absorption spectroscopy (IRAS), as previously reported by Waluyo and colleagues[45]. With this calibration, we can deposit ice films with an uncertainty in the adsorbed amount of less than 5%. During the TPD measurements, the adsorbed amount at each temperature can be derived from integration of the desorption flux[32].

Preparation of the HDO source. In the present study we deposited isotopically diluted HDO to simplify the spectral shape of the OH-stretch mode[47,48]. A D_2O water sample with a purity of 99.96 at% D purchased from ISOTEC and H_2O (milli-Q) were mixed with a ratio of 4:1 to obtain H-diluted HDO water samples with an isotope ratio of $[H_2O]:[HDO]:[D_2O] \sim 1:8:16$ (refs 49,50). Water samples were carefully pre-degassed in a UHV gas line by repeated freeze-pump-thaw cycles.

Apparatus set-up and experimental conditions. Experiments were performed in a UHV chamber combined with an optical system for IR-VIS SFG spectroscopy, which is described in detail elsewhere[24,51]. Briefly, the output pulse of a Ti:sapphire regenerative amplifier (Spectra Physics, 1 kHz, $\sim$2 mJ/pulse) was split into two to

generate a narrow band 800 nm 'visible' pulse ($\sim$0.5 µJ/pulse) and a broadband IR pulse (150-fs duration, $\sim$10 µJ/pulse, centred at $\sim$3,300 cm^{-1}) that covers almost the entire range of the hydrogen-bonded local OH-stretching band of HDO crystalline ice. The uncertainty in the intensity for the observed SFG spectra is less than 10% (Supplementary Fig. 5b), which is mainly due to the fluctuation of the incident laser pulses. Because of the strong reduction of the s-polarization field by the Fresnel coefficients, the ssp-SFG signal is much weaker than ppp-SFG signal for adsorbate on metal surfaces (Supplementary Section 1), which was also confirmed for $\sim$100 ML ice films on Pt(111) and Rh(111). We thus measured homodyne- and heterodyne-detected ppp-SFG spectra during the crystalline-ice film growth (Fig. 2) and the following TPD (Fig. 4) by coaxially aligned visible and infrared laser pulses with p-polarization at an incidence angle of 62°. It should be noted that our ppp-SFG spectra for ice films on a metal surface are dominated by the zzz component of effective ppp second-order nonlinear susceptibility: $\chi^{(2)}_{zzz}$ (Supplementary Section 1). For phase-sensitive SFG with heterodyne detection, we modified our previous optical set-up[24,51] to employ the 'collinear geometry' reported in ref. 22.

Data availability. The data that support the plots within this Article and other findings of this study are available from the corresponding author upon reasonable request.

References

39. Haq, S., Harnett, J. & Hodgson, A. Growth of thin crystalline ice films on Pt(111). *Surf. Sci.* **505,** 171–182 (2002).
40. Daschbach, J. L., Peden, B. M., Smith, R. S. & Kay, B. D. Adsorption, desorption, and clustering of H_2O on Pt(111). *J. Chem. Phys.* **120,** 1516–1523 (2004).
41. Lilach, Y., Iedema, M. J. & Cowin, J. P. Dissociation of water buried under ice on Pt(111). *Phys. Rev. Lett.* **98,** 016105 (2007).
42. Lilach, Y., Iedema, M. J. & Cowin, J. P. Reply to comment on 'Dissociation of water buried under ice on Pt(111)'. *Phys. Rev. Lett.* **99,** 109602 (2007).
43. Lilach, Y., Iedema, M. J. & Cowin, J. P. Proton segregation on a growing ice interface. *Surf. Sci.* **602,** 2886–2893 (2008).
44. Zimbitas, G., Gallagher, M. E., Darling, G. R. & Hodgson, A. Wetting of mixed OH and H_2O layers on Pt(111). *J. Chem. Phys.* **128,** 074701 (2008).
45. Waluyo, I. *et al.* Spectroscopic evidence for the formation of 3-D crystallites during isothermal heating of amorphous ice on Pt(111). *Surf. Sci.* **602,** 2004–2008 (2008).
46. Standop, S., Redinger, A., Morgenstern, M., Michely, T. & Busse, C. Molecular structure of the H_2O wetting layer on Pt(111). *Phys. Rev. B* **82,** 161412 (2010).
47. Sovago, M. *et al.* Vibrational response of hydrogen-bonded interfacial water is dominated by intramolecular coupling. *Phys. Rev. Lett.* **100,** 173901 (2008).
48. Nihonyanagi, S., Yamaguchi, S. & Tahara, T. Water hydrogen bond structure near highly charged interfaces is not like ice. *J. Am. Chem. Soc.* **132,** 6867–6869 (2010).
49. Pyper, J. W. & Newbury, R. S. Hydrogen–deuterium self-exchange in hydrogen sulfide and hydrogen selenide as studied with a pulsed-molecular-beam quadrupole mass filter. *J. Chem. Phys.* **52,** 1966–1971 (1970).
50. Kakiuchi, M. Distribution of isotopic water molecules, H_2O, HDO, and D_2O, in vapor and liquid phases in pure water and aqueous solution systems. *Geochim. Cosmochim. Acta* **64,** 1485–1492 (2000).
51. Inoue, K.-I., Watanabe, K. & Matsumoto, Y. Instantaneous vibrational frequencies of diffusing and desorbing adsorbates: CO/Pt(111). *J. Chem. Phys.* **137,** 024704 (2012).